AIAA JOURNAL
Vol. 40, No. 11, November 2002

Free Vibration Analysis of Rotating Cantilever Plates

Hong Hee Yoo*
Hanyang University, Seoul 133-791, Republic of Korea
and
Sung Kyun Kim†
Korea Atomic Energy Research Institute, Daejeon 305-353, Republic of Korea

Linearized equations of motion for the free vibration analysis of rotating cantilever plates are derived. Two in-plane stretch variables are introduced and approximated to obtain the ordinary differential equations of motion. The use of the two in-plane stretch variables enables one to obtain the equations of motion, which include proper motion-induced stiffness variation terms. The equations of motion are transformed into dimensionless forms in which dimensionless parameters are identified. The effects of the dimensionless parameters on the modal characteristics of rotating cantilever plates are investigated through numerical study. The eigenvalue loci veering and crossing along with the associated mode shape variations are also presented and discussed.

Nomenclature

A	=	reference frame of plate
a	=	length of plate
$\boldsymbol{a}^P$	=	acceleration of the generic point P
$\hat{\boldsymbol{a}}_1, \hat{\boldsymbol{a}}_2, \hat{\boldsymbol{a}}_3$	=	unit vector triad fixed to reference frame A
b	=	width of plate
D	=	bending rigidity of plate
E	=	Young's modulus
E_1	=	in-plane stretching rigidity of plate
E_2	=	in-plane shear rigidity of plate
F_i	=	generalized active force
F_i^*	=	generalized inertia force
G	=	shear modulus
h	=	thickness of plate
$\boldsymbol{K}$	=	stiffness matrix
$\boldsymbol{M}$	=	mass matrix
q_j	=	generalized coordinate
R	=	hub radius of rotation
s, r	=	in-plane stretch variables
T	=	reference time
U	=	total strain energy of rectangular plate
U_b	=	bending strain energy of rectangular plate
U_i	=	in-plane strain energy of rectangular plate
$\boldsymbol{u}$	=	displacement vector
u_1, u_2, u_3	=	measuring numbers of displacement vector in $\hat{a}_1$, $\hat{a}_2$, and $\hat{a}_3$ directions
$\boldsymbol{v}^P$	=	velocity of the generic point P
x, y	=	measuring numbers of the position vector (from reference point to generic point) before deformation
$\boldsymbol{Z}$	=	constant vector characterizing deflection shape for synchronous motion
$\boldsymbol{z}$	=	column matrix whose elements are z_j
z_j	=	dimensionless generalized coordinate
γ	=	dimensionless angular speed
δ	=	aspect ratio of plate (width to length)
ζ	=	dimensionless form of y
θ	=	setting angle
μ	=	sum of μ_1, μ_2, and μ_3
μ_1, μ_2, μ_3	=	numbers of generalized coordinates for s, r, and u_3
ν	=	Poisson's ratio
ρ	=	mass per unit area of plate
σ	=	ratio of hub radius to plate length
τ	=	dimensionless time
$\phi_{1i}, \phi_{2i}, \phi_{3i}$	=	spatial mode functions for s, r, and u_3
χ	=	dimensionless form of x
ψ_i	=	mode function of χ and ζ
Ω	=	constant angular speed of the hub
ω	=	dimensionless natural frequency

Subscript and Superscripts

$, x$	=	partial derivative of a symbol with respect to x
$\dot{}$	=	differentiation of a symbol with respect to time
$\ddot{}$	=	double differentiation of a symbol with respect to time

Received 20 May 2001; revision received 12 March 2002; accepted for publication 8 July 2002.

*Professor, School of Mechanical Engineering, Sungdong-Gu Haengdang-Dong 17; hhyoo@hanyang.ac.kr. Member AIAA.

†Researcher, TRIGA Research Reactor Decontamination and Decommissioning Team, Dukjin-Dong 150, Yousung-Gu; sungkyun@kaeri.re.kr.

I. Introduction

IT is well known that modal characteristics of rotating structures vary significantly compared to those of nonrotating structures. The radial rotating motion of a cantilever beam is a well-known example, where centrifugal inertia force results in the increase of system bending stiffness and effectively increases the natural frequencies. The phenomenon, often referred to as the motion-induced stiffening effect, has been investigated by many researchers because of its practical importance in engineering, for example, for turbine blades, turbomachine blades, and aircraft blades. For proper design of the structures, their modal characteristics should be accurately estimated as well as fully comprehended.

Rotating blades are often idealized as rotating beams because such idealization usually enables one to estimate the accurate modal characteristics of the structures. Study on the vibration of a rotating beam was pioneered by Southwell and Gough[1] in the early 1920s. They introduced a simple algebraic equation (which is often referred to as the Southwell equation) to calculate the natural frequencies of a rotating beam based on the Rayleigh energy theorem. This equation is still being used by many engineers due to its excellent simplicity and reliability. Later, to increase the accuracy of the Southwell equation, Schilhansl[2] derived a partial differential equation of a rotating beam and applied the Ritz method to the equation to obtain more accurate coefficients for the Southwell equation. These rather analytical methods (to estimate the modal characteristics of rotating blades) were followed by numerical methods as computers could be exploited. More complex shapes and sophisticated effects of rotating blades could be considered with the numerical methods. A large number of papers that employ numerical methods for modal

analysis of rotating blades have been published. Survey papers, for instance, Refs. 3 and 4 are also available.

As the aspect ratio of a blade decreases, the blade behaves like a plate rather than a beam. Therefore, for a blade with low aspect ratio, it is not proper to employ a beam theory to predict its modal characteristics. Obviously, a plate theory needs to be employed to predict the modal characteristics of a blade with low aspect ratio. There are, however, only a few available papers on the modal characteristics of a rotating plate (according to a literature survey conducted by the present authors). Dokainish and Rawtani[5] used a finite element technique to determine the modal characteristics of rotating cantilever plates. A similar approach was taken by Ramamurti and Kielb[6] to determine the modal characteristics of a twisted rotating plate. They used a strain energy expression for a plate that employs steady-state in-plane stress components. The steady-state in-plane stress components were obtained either analytically from the partial differential equations of stretching motion or numerically from the equilibrium condition between the centrifugal inertia force and the steady-state in-plane stress. Then, the equations of motion were derived by using the strain energy expression in which the steady-state in-plane stress components previously obtained were employed. Because of the prohibitive complexities involved in this conventional modeling method, the procedure of deriving equations of motion was rarely described in detail in the literature.

Different from the conventional modeling method, which employs only Cartesian deformation variables, a new modeling method for beams undergoing overall motion was introduced by Kane et al.[7] and later extended by Yoo et al.[8] This modeling method employs a non-Cartesian deformation variable that represents the stretch of the beam along its neutral axis to derive equations of motion directly. The use of the non-Cartesian variable led to the accurate capture of the stiffening effect. This modeling method was later successfully utilized to obtain the modal characteristics of rotating beams by Yoo and Shin.[9] Similarly, a linear dynamic modeling method for plates undergoing overall motion was introduced by Yoo,[10] and its accuracy was verified by Yoo and Chung.[11] A similar modeling method was also developed for another two-dimensional elastic body, a disk, by Flowers.[12] The key ingredient of the modeling method introduced in Refs. 10 and 11 is the use of two in-plane stretch variables by which the exact in-plane strain energy can be expressed in a quadratic form. The use of the two stretch variables enables one to derive linearized equations of motion that include proper motion-induced stiffness variation terms. In these works, however, mostly transient characteristics of rotating plates were investigated.

The purpose of the present paper is to investigate the modal characteristics of rotating cantilever plates that are attached to a rigid hub with a setting angle. The dynamic modeling method, which was introduced in Refs. 10 and 11 for plates undergoing overall motion, is employed to derive the modal equations of the rotating cantilever plate. The modal equations are then transformed into dimensionless forms, in which dimensionless parameters are identified. The effects of the dimensionless parameters on the modal characteristics of rotating cantilever plates are investigated through numerical study.

II. Equations of Motion

Figure 1 shows a cantilever plate that is attached to a rigid hub (with radius R) with a setting angle θ. The plate is characterized by natural length a; width b; thickness h; and material properties E, Young's modulus; G, shear modulus; ρ, mass per unit area; and ν, Poisson's ratio. The transverse shear and the rotary inertia effects are not considered. Those effects were previously investigated for nonrotating plates by many researchers. If considered here, the effects will complicate the formulation, only to produce results that are essentially the same as those found by previous researchers. Therefore, in the present work, the Kirchhoff hypothesis is employed to simplify the formulation. Based on the Kirchhoff hypothesis, any straight line segments perpendicular to the midplane of the plate remain perpendicular to the midplane during the deformation. A coordinate system (which consists of three mutually orthogonal unit vectors $\hat{\boldsymbol{a}}_1$, $\hat{\boldsymbol{a}}_2$, and $\hat{\boldsymbol{a}}_3$) is fixed to the straight line segment that is located in the middle of the fixed boundary. Here, $\hat{\boldsymbol{a}}_1$ is parallel to the length of the plate, $\hat{\boldsymbol{a}}_2$ is parallel to the width of the plate, and

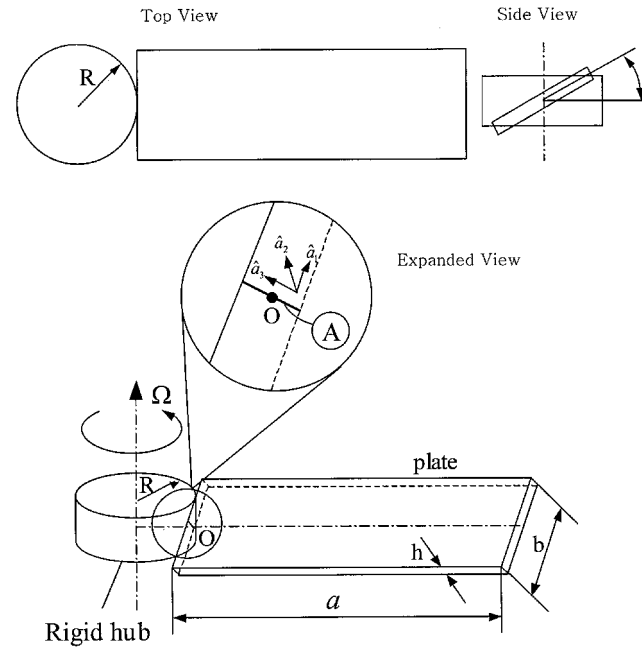

Fig. 1 Configuration of a cantilever plate attached to a rigid hub at a setting angle θ.

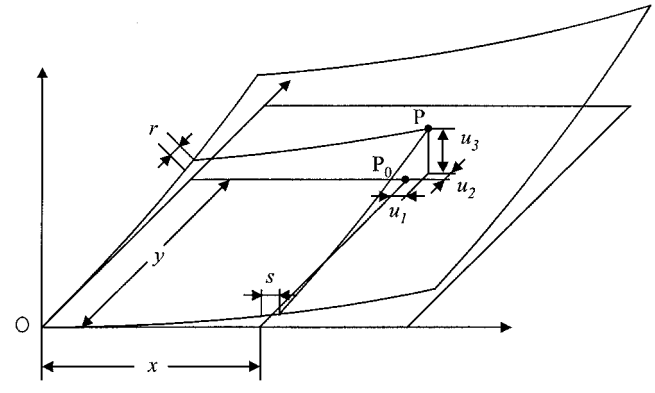

Fig. 2 Deformation of the midplane of a plate.

$\hat{\boldsymbol{a}}_3$ is parallel to the straight line segment. The reference frame (the rigid hub) A is assumed to rotate with a constant angular speed Ω. If $\hat{\boldsymbol{a}}_3$ is the direction of rotation, the setting angle is zero. A more general configuration of a plate having nonzero setting angle can be obtained by rotating the plate around $\hat{\boldsymbol{a}}_1$. More general configurations involved with taper angle, stagger angle, and negative hub radius are not investigated in the present work.

The angular velocity of the reference frame and the velocity of a point O (which is the reference point of the coordinate system) can be expressed as follows:

$$\boldsymbol{\omega}^A = \Omega(\sin\theta\hat{\boldsymbol{a}}_2 + \cos\theta\hat{\boldsymbol{a}}_3) \tag{1}$$

$$\boldsymbol{v}^O = R\Omega(\cos\theta\hat{\boldsymbol{a}}_2 - \sin\theta\hat{\boldsymbol{a}}_3) \tag{2}$$

Figure 2 shows the deformation of the midplane of a plate, where x and y are the distances measured from the reference point O to a generic point P_0 (which lies on the midplane of undeformed plate) along directions of $\hat{\boldsymbol{a}}_1$ and $\hat{\boldsymbol{a}}_2$, respectively. When the plate is deformed, point P_0 moves to a new point P. The displacement vector from P_0 to P is $\boldsymbol{u}$ and is expressed as follows:

$$\boldsymbol{u} = u_1\hat{\boldsymbol{a}}_1 + u_2\hat{\boldsymbol{a}}_2 + u_3\hat{\boldsymbol{a}}_3 \tag{3}$$

Conventionally, the three Cartesian variables u_1, u_2, and u_3 are approximated to obtain the ordinary differential equations of motion. In the present work, two in-plane stretch variables (s and r shown in Fig. 2) along with the lateral displacement u_3 are approximated.

Thus, by the use of the Rayleigh–Ritz method, they can be expressed as follows:

$$s(x, y, t) = \sum_{j=1}^{\mu} \phi_{1j}(x, y) q_j(t) \tag{4}$$

$$r(x, y, t) = \sum_{j=1}^{\mu} \phi_{2j}(x, y) q_j(t) \tag{5}$$

$$u_3(x, y, t) = \sum_{j=1}^{\mu} \phi_{3j}(x, y) q_j(t) \tag{6}$$

Any compact set of admissible functions that satisfies the geometric boundary conditions of the plate can be used as the mode functions.[13] Here μ is the total number of the generalized coordinates. For the convenience of formalism, s, r, and u_3 use the same number of coordinates μ. However, they are not actually coupled. For instance, ϕ_{1j} is not zero only if $j \le \mu_1$; ϕ_{2j} is not zero only if $\mu_1 < j \le \mu_1 + \mu_2$; and ϕ_{3j} is not zero only if $\mu_1 + \mu_2 < j \le \mu_1 + \mu_2 + \mu_3$. In other words, μ_1, μ_2, and μ_3 denote the actual numbers of generalized coordinates for s, r, and u_3, respectively, and μ is the total sum of μ_1, μ_2, and μ_3.

When the two stretch variables s and r are used, the following expression of in-plane strain energy of a rectangular plate can be obtained:

$$U_i = \frac{1}{2} \int_{-b/2}^{b/2} \int_0^a \left\{ E_1 \left[\left(\frac{\partial s}{\partial x} \right)^2 + \left(\frac{\partial r}{\partial y} \right)^2 + 2\nu \left(\frac{\partial s}{\partial x} \right) \left(\frac{\partial r}{\partial y} \right) \right] + E_2 \left(\frac{\partial s}{\partial y} + \frac{\partial r}{\partial x} \right)^2 \right\} \mathrm{d}x\, \mathrm{d}y \tag{7}$$

where

$$E_1 = Eh/(1 - \nu^2) \tag{8}$$

$$E_2 = Gh \tag{9}$$

If the Cartesian variables u_1 and u_2 instead of s and r are substituted into Eq. (7), the conventional approximate form of in-plane strain energy of a plate can be obtained. When the bending strain energy and the in-plane strain energy are added, the total strain energy can be obtained as follows:

$$U = U_i + U_b \tag{10}$$

where U_b represents the bending strain energy, which is given by

$$U_b = \frac{1}{2} \int_{-b/2}^{b/2} \int_0^a D \left[\left(\frac{\partial^2 u_3}{\partial x^2} \right)^2 + \left(\frac{\partial^2 u_3}{\partial y^2} \right)^2 + 2\nu \left(\frac{\partial^2 u_3}{\partial x^2} \right) \left(\frac{\partial^2 u_3}{\partial y^2} \right) + 2(1 - \nu) \left(\frac{\partial^2 u_3}{\partial x \partial y} \right)^2 \right] \mathrm{d}x\, \mathrm{d}y \tag{11}$$

where

$$D = Eh^3/12(1 - \nu^2) \tag{12}$$

The present work employs Kane's method (see Kane and Levinson[14]) in which the generalized active forces and generalized inertia forces need to be obtained to derive the equations of motion. Because external active forces need not be considered for the free vibration analysis, the generalized active forces can be obtained as follows:

$$F_i = -\frac{\partial U}{\partial q_i} \qquad (i = 1, 2, \ldots, \mu) \tag{13}$$

Because the total strain energy U has a quadratic form, the generalized active forces are linear. Now the generalized inertia forces can be obtained by using the following equation:

$$F_i^* = -\int_{-b/2}^{b/2} \int_0^a \rho \left(\frac{\partial \boldsymbol{v}^P}{\partial \dot{q}_i} \right) \cdot \boldsymbol{a}^P \, \mathrm{d}x\, \mathrm{d}y \qquad (i = 1, 2, \ldots, \mu) \tag{14}$$

where $\dot{q}_i$ are the time derivatives of the generalized coordinates. When the angular velocity of the reference frame A and the velocity of the point O are used, the velocity of the generic point P can be obtained as follows:

$$\begin{aligned} \boldsymbol{v}^P = {} & [\dot{u}_1 + \Omega \sin\theta u_3 - \Omega \cos\theta (y + u_2)] \hat{\boldsymbol{a}}_1 \\ & + [R\Omega \cos\theta + \dot{u}_2 + \Omega \cos\theta (x + u_1)] \hat{\boldsymbol{a}}_2 \\ & + [-R\Omega \sin\theta + \dot{u}_3 - \Omega \sin\theta (x + u_1)] \hat{\boldsymbol{a}}_3 \end{aligned} \tag{15}$$

Because u_1, u_2, and their derivatives with respect to time shown in Eq. (15) are not to be approximated, they need to be replaced by s, r, u_3, and their derivatives. For the replacement, the following geometric relations[15] can be used:

$$x + s = \int_0^x \left[\left(1 + \frac{\partial u_1}{\partial \xi} \right)^2 + \left(\frac{\partial u_3}{\partial \xi} \right)^2 \right]^{\frac{1}{2}} \mathrm{d}\xi \tag{16}$$

$$y + r = \int_0^y \left[\left(1 + \frac{\partial u_2}{\partial \eta} \right)^2 + \left(\frac{\partial u_3}{\partial \eta} \right)^2 \right]^{\frac{1}{2}} \mathrm{d}\eta \tag{17}$$

In the present work, the equations of motion will be linearized eventually. Only up to second-degree terms need to be retained in the geometric relations because the final form of equations of motion is not affected by the truncated higher degree terms. Therefore, the following approximated relations, which are obtained by using the binomial expansion of Eqs. (16) and (17), can be used:

$$s = u_1 + \frac{1}{2} \int_0^x \left[\left(\frac{\partial u_3}{\partial \xi} \right)^2 \right] \mathrm{d}\xi \tag{18}$$

$$r = u_2 + \frac{1}{2} \int_0^y \left[\left(\frac{\partial u_3}{\partial \eta} \right)^2 \right] \mathrm{d}\eta \tag{19}$$

Differentiations of Eqs. (18) and (19) with respect to time yield

$$\dot{s} = \dot{u}_1 + \int_0^x \left[\left(\frac{\partial \dot{u}_3}{\partial \xi} \right) \left(\frac{\partial u_3}{\partial \xi} \right) \right] \mathrm{d}\xi \tag{20}$$

$$\dot{r} = \dot{u}_2 + \int_0^y \left[\left(\frac{\partial \dot{u}_3}{\partial \eta} \right) \left(\frac{\partial u_3}{\partial \eta} \right) \right] \mathrm{d}\eta \tag{21}$$

When Eqs. (20) and (21) are used along with Eqs. (15) and (4–6), the partial derivative of $\boldsymbol{v}^P$ with respect to $\dot{q}_i$ can be obtained as follows:

$$\begin{aligned} \frac{\partial \boldsymbol{v}^P}{\partial \dot{q}_i} = {} & \left[\phi_{1i} - \sum_{j=1}^{\mu} \int_0^x \phi_{3i,\xi} \phi_{3j,\xi} \, \mathrm{d}\xi q_j \right] \hat{\boldsymbol{a}}_1 \\ & + \left[\phi_{2i} - \sum_{j=1}^{\mu} \int_0^y \phi_{3i,\eta} \phi_{3j,\eta} \, \mathrm{d}\eta q_j \right] \hat{\boldsymbol{a}}_2 + \phi_{3i} \hat{\boldsymbol{a}}_3 \end{aligned} \tag{22}$$

These partial velocities and the acceleration of point P, which can be obtained simply by differentiating the velocity shown in Eq. (15) with respect to time, are substituted into Eq. (14) to obtain the generalized inertia forces. When the generalized inertia forces are linearized and the generalized active forces [obtained in Eq. (13)] are summed, the following linearized equations of motion can be obtained:

$$\begin{aligned} \sum_{j=1}^{\mu} \Big[& M_{ij}^{11} \ddot{q}_j - 2\Omega \cos\theta M_{ij}^{12} \dot{q}_j + 2\Omega \sin\theta M_{ij}^{13} \dot{q}_j + \left(K_{ij}^{S1} + K_{ij}^{S2} \right) q_j \\ & - \Omega^2 M_{ij}^{11} q_j \Big] = \Omega^2 X_{1i} + R\Omega^2 Z_{1i} \end{aligned} \tag{23}$$

$$\begin{aligned} \sum_{j=1}^{\mu} \Big[& M_{ij}^{22} \ddot{q}_j + 2\Omega \cos\theta M_{ij}^{21} \dot{q}_j + \left(K_{ij}^{S3} + K_{ij}^{S4} \right) q_j \\ & + \Omega^2 \cos\theta \sin\theta M_{ij}^{23} q_j - \Omega^2 \cos^2\theta M_{ij}^{22} q_j \Big] = \Omega^2 \cos^2\theta Y_{2i} \end{aligned} \tag{24}$$

$$\sum_{j=1}^{\mu}\Big[M_{ij}^{33}\ddot{q}_j - 2\Omega\sin\theta M_{ij}^{31}\dot{q}_j + K_{ij}^{B}q_j + \Omega^2 K_{ij}^{GX2}q_j + \Omega^2\cos^2\theta K_{ij}^{GY2}q_j + R\Omega^2 K_{ij}^{GX1}q_j + \Omega^2\cos\theta\sin\theta M_{ij}^{32}q_j - \Omega^2\sin^2\theta M_{ij}^{33}q_j\Big] = -\Omega^2\cos\theta\sin\theta Y_{3i} \tag{25}$$

where

$$M_{ij}^{lm} = \int_{-b/2}^{b/2}\int_0^a \rho\phi_{li}\phi_{mj}\,dx\,dy \tag{26}$$

$$K_{ij}^{S1} = \int_{-b/2}^{b/2}\int_0^a (E_1\phi_{1i,x}\phi_{1j,x} + E_2\phi_{1i,y}\phi_{1j,y})\,dx\,dy \tag{27}$$

$$K_{ij}^{S2} = \int_{-b/2}^{b/2}\int_0^a (E_1\nu\phi_{1i,x}\phi_{2j,y} + E_2\phi_{1i,y}\phi_{2j,x})\,dx\,dy \tag{28}$$

$$K_{ij}^{S3} = \int_{-b/2}^{b/2}\int_0^a (E_1\phi_{2i,y}\phi_{2j,y} + E_2\phi_{2i,x}\phi_{2j,x})\,dx\,dy \tag{29}$$

$$K_{ij}^{S4} = \int_{-b/2}^{b/2}\int_0^a (E_1\nu\phi_{2i,y}\phi_{1j,x} + E_2\phi_{2i,x}\phi_{1j,y})\,dx\,dy \tag{30}$$

$$K_{ij}^{B} = \int_{-b/2}^{b/2}\int_0^a D[\phi_{3i,xx}\phi_{3j,xx} + \phi_{3i,yy}\phi_{3j,yy} + \nu\phi_{3i,xx}\phi_{3j,yy} + \nu\phi_{3i,yy}\phi_{3j,xx} + 2(1-\nu)\phi_{3i,xy}\phi_{3j,xy}]\,dx\,dy \tag{31}$$

$$K_{ij}^{GX2} = \int_{-b/2}^{b/2}\int_0^a \frac{1}{2}\rho(a^2-x^2)\phi_{3i,x}\phi_{3j,x}\,dx\,dy \tag{32}$$

$$K_{ij}^{GX1} = \int_{-b/2}^{b/2}\int_0^a \rho(a-x)\phi_{3i,x}\phi_{3j,x}\,dx\,dy \tag{33}$$

$$K_{ij}^{GY2} = \int_{-b/2}^{b/2}\int_0^a \frac{1}{2}\rho\left(\frac{b^2}{4}-y^2\right)\phi_{3i,y}\phi_{3j,y}\,dx\,dy \tag{34}$$

$$X_{mi} = \int_{-b/2}^{b/2}\int_0^a \rho(R+x)\phi_{mi}\,dx\,dy \tag{35}$$

$$Y_{mi} = \int_{-b/2}^{b/2}\int_0^a \rho y\phi_{mi}\,dx\,dy \tag{36}$$

$$Z_{mi} = \int_{-b/2}^{b/2}\int_0^a \rho\phi_{mi}\,dx\,dy \tag{37}$$

It is useful to rewrite Eqs. (23–25) in a dimensionless form. The following dimensionless variables are introduced to obtain the dimensionless form of equations of motion:

$$\tau = t/T \tag{38}$$

$$\chi = x/a \tag{39}$$

$$\zeta = y/b \tag{40}$$

$$z_j = q_j/a \tag{41}$$

where T is defined as

$$T = (\rho h a^4/D)^{\frac{1}{2}} \tag{42}$$

The nonhomogeneous terms that appear in the right-hand side of Eqs. (23–25) are not necessary for the free vibration analysis. Therefore, the following dimensionless homogeneous equations will be used:

$$\sum_{j=1}^{\mu}\Big[\bar{M}_{ij}^{11}\ddot{z}_j - 2\gamma\cos\theta\bar{M}_{ij}^{12}\dot{z}_j + 2\gamma\sin\theta\bar{M}_{ij}^{13}\dot{z}_j + \big(\bar{K}_{ij}^{S1}+\bar{K}_{ij}^{S2}\big)z_j - \gamma^2\bar{M}_{ij}^{11}z_j\Big] = 0 \tag{43}$$

$$\sum_{j=1}^{\mu}\Big[\bar{M}_{ij}^{22}\ddot{z}_j + 2\gamma\cos\theta\bar{M}_{ij}^{21}\dot{z}_j + \big(\bar{K}_{ij}^{S3}+\bar{K}_{ij}^{S4}\big)z_j - \gamma^2\cos^2\theta\bar{M}_{ij}^{22}z_j + \gamma^2\cos\theta\sin\theta\bar{M}_{ij}^{23}z_j\Big] = 0 \tag{44}$$

$$\sum_{j=1}^{\mu}\Big[\bar{M}_{ij}^{33}\ddot{z}_j - 2\gamma\sin\theta\bar{M}_{ij}^{31}\dot{z}_j + \bar{K}_{ij}^{B}z_j + \gamma^2\bar{K}_{ij}^{GX2}z_j + \gamma^2\cos^2\theta\bar{K}_{ij}^{GY2}z_j + \sigma\gamma^2\bar{K}_{ij}^{GX1}z_j + \gamma^2\cos\theta\sin\theta\bar{M}_{ij}^{32}z_j - \gamma^2\sin^2\theta\bar{M}_{ij}^{33}z_j\Big] = 0 \tag{45}$$

where a dot over a symbol now means differentiation with respect to τ and

$$\bar{M}_{ij}^{\alpha\beta} = \int_{-\frac{1}{2}}^{\frac{1}{2}}\int_0^1 \psi_{\alpha i}\psi_{\beta j}\,d\chi\,d\zeta \tag{46}$$

$$\bar{K}_{ij}^{S1} = \int_{-\frac{1}{2}}^{\frac{1}{2}}\int_0^1 \left(\frac{E_1T^2}{\rho a^2}\psi_{1i,\chi}\psi_{1j,\chi} + \frac{E_2T^2}{\rho b^2}\psi_{1i,\zeta}\psi_{1j,\zeta}\right)d\chi\,d\zeta \tag{47}$$

$$\bar{K}_{ij}^{S2} = \int_{-\frac{1}{2}}^{\frac{1}{2}}\int_0^1 \left(\frac{E_1T^2}{\rho ab}\nu\psi_{1i,\chi}\psi_{2j,\zeta} + \frac{E_2T^2}{\rho ab}\psi_{1i,\zeta}\psi_{2j,\chi}\right)d\chi\,d\zeta \tag{48}$$

$$\bar{K}_{ij}^{S3} = \int_{-\frac{1}{2}}^{\frac{1}{2}}\int_0^1 \left(\frac{E_1T^2}{\rho b^2}\psi_{2i,\zeta}\psi_{2j,\zeta} + \frac{E_2T^2}{\rho a^2}\psi_{2i,\chi}\psi_{2j,\chi}\right)d\chi\,d\zeta \tag{49}$$

$$\bar{K}_{ij}^{S4} = \int_{-\frac{1}{2}}^{\frac{1}{2}}\int_0^1 \left(\frac{E_1T^2}{\rho ab}\nu\psi_{2i,\zeta}\psi_{1j,\chi} + \frac{E_2T^2}{\rho ab}\psi_{2i,\chi}\psi_{1j,\zeta}\right)d\chi\,d\zeta \tag{50}$$

$$\bar{K}_{ij}^{B} = \int_{-\frac{1}{2}}^{\frac{1}{2}}\int_0^1 \big[\psi_{3i,\chi\chi}\psi_{3j,\chi\chi} + \delta^4\psi_{3i,\zeta\zeta}\psi_{3j,\zeta\zeta} + \nu\delta^2\psi_{3i,\chi\chi}\phi_{3j,\zeta\zeta} + \nu\delta^2\psi_{3i,\zeta\zeta}\psi_{3j,\chi\chi} + 2(1-\nu)\delta^2\psi_{3i,\chi\zeta}\psi_{3j,\chi\zeta}\big]\,d\chi\,d\zeta \tag{51}$$

$$\bar{K}_{ij}^{GX2} = \int_{-\frac{1}{2}}^{\frac{1}{2}}\int_0^1 \frac{1}{2}(1-\chi^2)\psi_{3i,\chi}\psi_{3j,\chi}\,d\chi\,d\zeta \tag{52}$$

$$\bar{K}_{ij}^{GY2} = \int_{-\frac{1}{2}}^{\frac{1}{2}}\int_0^1 \frac{1}{2}\left(\frac{1}{4}-\zeta^2\right)\psi_{3i,\zeta}\psi_{3j,\zeta}\,d\chi\,d\zeta \tag{53}$$

$$\bar{K}_{ij}^{GX1} = \int_{-\frac{1}{2}}^{\frac{1}{2}}\int_0^1 (1-\chi)\psi_{3i,\chi}\psi_{3j,\chi}\,d\chi\,d\zeta \tag{54}$$

The function ψ_{ij} (shown in the preceding equations), which is the function of dimensionless variables χ and ζ, has the same numerical value as the function ϕ_{ij}, which is the function of x and y.

There are three parameters involved in Eqs. (43–45): δ, the ratio of the plate width to its length (the aspect ratio); σ, the ratio of the hub radius to the plate length; and γ, the dimensionless angular speed. These parameters are given as follows:

$$\delta = a/b \tag{55}$$

$$\sigma = R/a \tag{56}$$

$$\gamma = \Omega T \tag{57}$$

Table 1 Convergence of dimensionless natural frequencies vs number of modes[a]

Total number of modes (number of X modes × number of Y modes)	First frequency	Second frequency	Third frequency	Fourth frequency	Fifth frequency
15 (3×5)	10.037	32.997	69.712	73.243	207.564
24 (4×6)	10.019	32.905	68.360	73.143	132.004
35 (5×7)	10.010	32.864	68.141	72.933	131.633
42 (6×7)	10.005	32.844	67.760	72.923	131.523
49 (7×7)	10.001	32.835	67.657	72.888	131.518
63 (7×9)	10.001	32.832	67.657	72.880	131.509

[a]Values of $\delta = 10$, $\sigma = 0$, $\gamma = 10$, and $\theta = 30$ deg.

Using Eqs. (43–45), a matrix form of the equations of motion is obtained as follows:

$$\boldsymbol{M}\ddot{\boldsymbol{z}} + \boldsymbol{C}\dot{\boldsymbol{z}} + \boldsymbol{K}\boldsymbol{z} = \boldsymbol{0} \tag{58}$$

where

$$\boldsymbol{M} = \begin{bmatrix} \bar{M}^{11} & 0 & 0 \\ 0 & \bar{M}^{22} & 0 \\ 0 & 0 & \bar{M}^{33} \end{bmatrix} \tag{59}$$

$$\boldsymbol{C} = \begin{bmatrix} 0 & -2\gamma\cos\theta\bar{M}^{12} & 2\gamma\sin\theta\bar{M}^{13} \\ 2\gamma\cos\theta\bar{M}^{21} & 0 & 0 \\ -2\gamma\sin\theta\bar{M}^{31} & 0 & 0 \end{bmatrix} \tag{60}$$

$$\boldsymbol{K} = \begin{bmatrix} K^{11} & K^{12} & K^{13} \\ K^{21} & K^{22} & K^{23} \\ K^{31} & K^{32} & K^{33} \end{bmatrix} \tag{61}$$

where the components of the element matrices in Eq. (61) are defined as follows:

$$K_{ij}^{11} = \bar{K}_{ij}^{S1} - \gamma^2\bar{M}_{ij}^{11}, \qquad K_{ij}^{12} = K_{ji}^{21} = \bar{K}_{ij}^{S2} = \bar{K}_{ji}^{S4}$$

$$K_{ij}^{13} = K_{ji}^{31} = 0, \qquad K_{ij}^{22} = \bar{K}_{ij}^{S3} - \gamma^2\cos^2\theta\bar{M}_{ij}^{22}$$

$$K_{ij}^{23} = K_{ji}^{32} = \gamma^2\cos\theta\sin\theta\bar{M}_{ij}^{23}$$

$$K_{ij}^{33} = \bar{K}_{ij}^{B} + \gamma^2\bar{K}_{ij}^{GX2} + \gamma^2\cos^2\theta\bar{K}_{ij}^{GY2} + \gamma^2\sigma\bar{K}_{ij}^{GX1} - \gamma^2\sin^2\theta\bar{M}_{ij}^{33} \tag{62}$$

Note that the equations are coupled through the gyroscopic damping matrix in Eq. (60) and the stiffness matrix in Eq. (61). To derive the eigenvalue problem, Eq. (58) is transformed into the following form:

$$\boldsymbol{M}^*\dot{\eta} + \boldsymbol{K}^*\eta = \boldsymbol{0} \tag{63}$$

where

$$\boldsymbol{M}^* = \begin{bmatrix} \boldsymbol{M} & \boldsymbol{0} \\ \boldsymbol{0} & \boldsymbol{I} \end{bmatrix} \tag{64}$$

$$\boldsymbol{K}^* = \begin{bmatrix} \boldsymbol{C} & \boldsymbol{K} \\ -\boldsymbol{I} & \boldsymbol{0} \end{bmatrix} \tag{65}$$

$$\eta = \begin{Bmatrix} \dot{z} \\ z \end{Bmatrix} \tag{66}$$

An eigenvalue problem can be derived by assuming that η is a harmonic matrix function of τ expressed as

$$\eta = e^{\lambda\tau}\Theta \tag{67}$$

where λ is the complex eigenvalue and Θ is the complex mode shape. Substituting Eq. (67) into Eq. (63) yields

$$\lambda\boldsymbol{M}^*\Theta + \boldsymbol{K}^*\Theta = 0 \tag{68}$$

The formulations presented in this section are employed to obtain the numerical results shown in the next section.

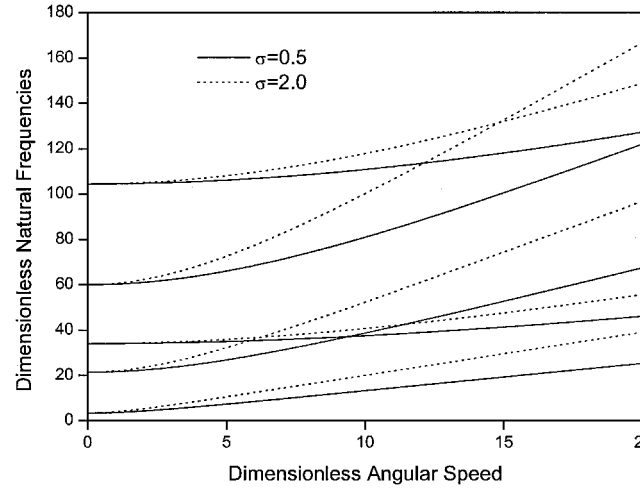

Fig. 3 Lowest five natural frequencies vs angular speed for two values of hub radius ratio with $\delta = 5$ and $\theta = 30$ deg.

III. Numerical Results

To solve the eigenvalue problem formulated in Eq. (68) for the rotating plate, assumed mode functions are needed. In the present work, 35 plate mode functions are employed to obtain the adequate convergence of a few of the lowest eigensolutions. The 35 plate mode functions are generated with 5 cantilever beam mode functions (for spanwise direction) and seven free–free beam mode functions (for chordwise direction), which include two rigid-body mode functions.[13] The convergence of the solution vs number of modes is shown in Table 1 for a set of typical dimensionless parameters (which are also shown). The results show that the use of 35 mode functions leads to the sufficiently converged solutions of the lowest 5 natural frequencies.

Figure 3 shows the variations of the lowest five dimensionless natural frequencies of rotating cantilever plates (with aspect ratio $\delta = 5$). The setting angle employed for Fig. 3 is 30 deg. The results shown by solid lines were obtained with relatively small hub radius ratio ($\sigma = 0.5$), whereas those shown by dotted lines were obtained with relatively large hub radius ratio ($\sigma = 2.0$). As expected intuitively, the natural frequencies increase as the angular speed increases. The larger hub radius ratio results in the stiffer slopes of the frequency loci. This is caused by the centrifugal inertia force, which increases as the angular speed and the hub radius increase.

Figure 4 shows the variations of the nodal lines of the lowest five mode shapes of a rectangular plate caused by rotating motion. The parameters employed to obtain the results are as follows: $\delta = 5$, $\sigma = 0.5$, and $\theta = 30$ deg. The dimensionless angular speed used for Fig. 4a is 0, and that for Fig. 4b is 10. It is shown in Fig. 4a that the first two modes represent the lowest two spanwise bending modes, that the third mode represents the first torsional mode, that the fourth mode represents the third spanwise bending mode, and that the fifth mode represents the first skew-symmetric combination mode (torsion plus spanwise bending). When Fig. 4b is compared to Fig. 4a, one can see that the second and third modes are switched. This mode switching results from the eigenvalue loci crossing shown in Fig. 3. Because the centrifugal inertia force influences the spanwise bending mode more than the torsional mode, the eigenvalue of the

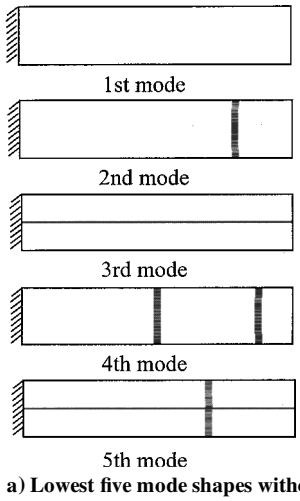

a) Lowest five mode shapes without rotation ($\gamma = 0$)

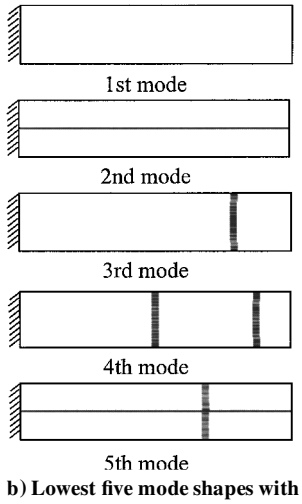

b) Lowest five mode shapes with rotation ($\gamma = 10$)

Fig. 4 Nodal line variations of the lowest five modes caused by the rotation; $\delta = 5$, $\sigma = 0.5$, and $\theta = 30$ deg.

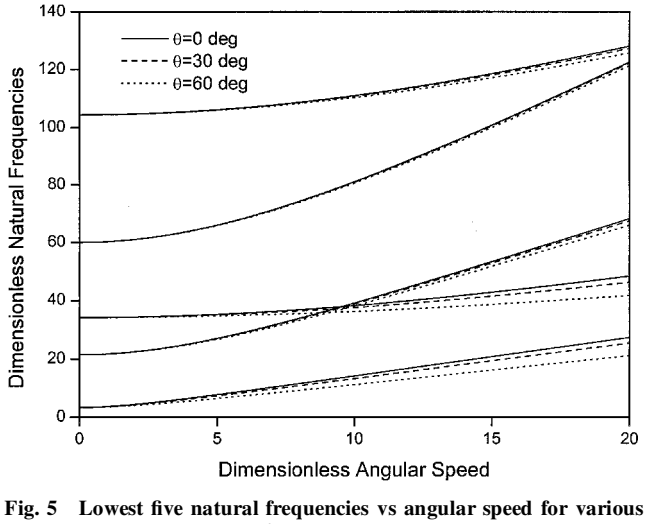

Fig. 5 Lowest five natural frequencies vs angular speed for various values of setting angles with $\delta = 5$ and $\sigma = 0.5$.

spanwise bending mode increases faster than that of the first torsional mode (as the angular speed increases). Thus, the eigenvalue loci crossing and the associated mode switching occur.

Figure 5 shows the effect of the setting angle on the variations of the lowest five dimensionless natural frequencies of rotating plates. The parameters employed for the results are $\delta = 5$ and $\sigma = 0.5$. The results shown by solid lines were obtained with $\theta = 0$ deg, those shown by broken solid lines were obtained with $\theta = 30$ deg, and those shown by dotted lines were obtained with

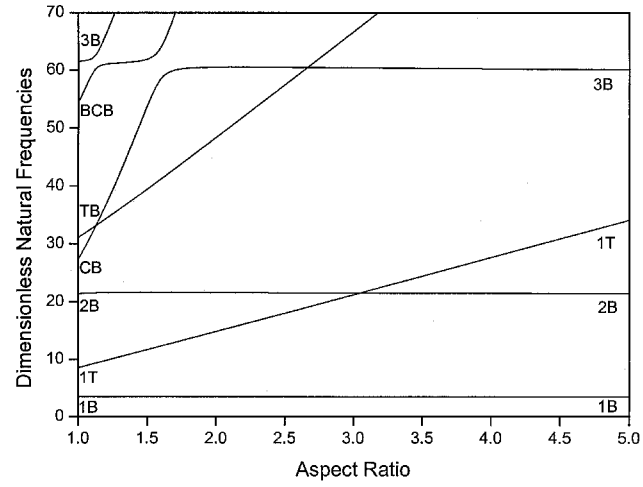

Fig. 6 Natural frequencies of a nonrotating plate vs aspect ratio.

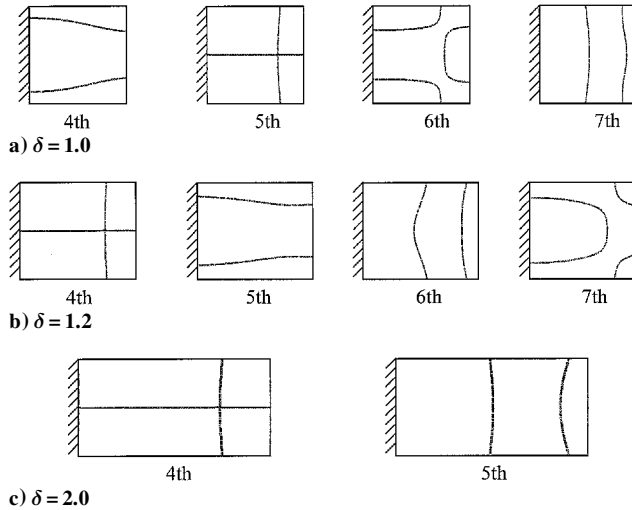

Fig. 7 Nodal line variations of fourth, fifth, sixth, and seventh mode shapes.

$\theta = 60$ deg. It is shown that all of the five natural frequencies are slightly lowered as the setting angle increases.

Figure 6 shows some lowest dimensionless natural frequencies of nonrotating plate vs aspect ratio. In Fig. 6, 1B, 2B, and 3B denote the first, second, and the third spanwise bending modes, 1T denotes the first torsional mode, CB denotes the chordwise bending mode, TB denotes the first skew-symmetric combination mode (torsion plus spanwise bending), and BCB denotes the first symmetric combination mode (spanwise bending plus chordwise bending). As the aspect ratio increases, some loci cross each other. The fourth and the fifth loci even cross twice (around $\delta = 1.1$ and 2.7). However, some loci veer: the fifth and the sixth around $\delta = 1.5$ and the sixth and the seventh around $\delta = 1.1$. Eigenvalue loci veering phenomena were previously observed in other engineering examples (see Refs. 16–18). In these examples, two eigenvalue loci approach each other closely. Hence, it was once mistakenly speculated that the phenomena resulted from numerical approximation. Apart from those close veering examples, the two loci around the veering regions in Fig. 6 are substantially separated from each other. Figures 7a–7c show the variations of mode shapes at $\delta = 1.0$ (fourth, fifth, sixth, and seventh), $\delta = 1.2$ (fourth, fifth, sixth, and seventh), and $\delta = 2.0$ (fourth and fifth), respectively. Because only the lowest five natural frequencies appear at $\delta = 2.0$ in Fig. 6, the fourth and the fifth mode shapes are given in Fig. 7c. Figure 7c clearly shows that the mode shape exchange occurs not only at the crossing region but also at the veering region. Note that the seventh mode at $\delta = 1.0$, the sixth mode at $\delta = 1.2$, and the fifth mode at $\delta = 2.0$ all represent the third bending mode. It can be also observed that a loci crossing occurs between skew-symmetric and symmetric modes, whereas a loci veering occurs between two symmetric modes.

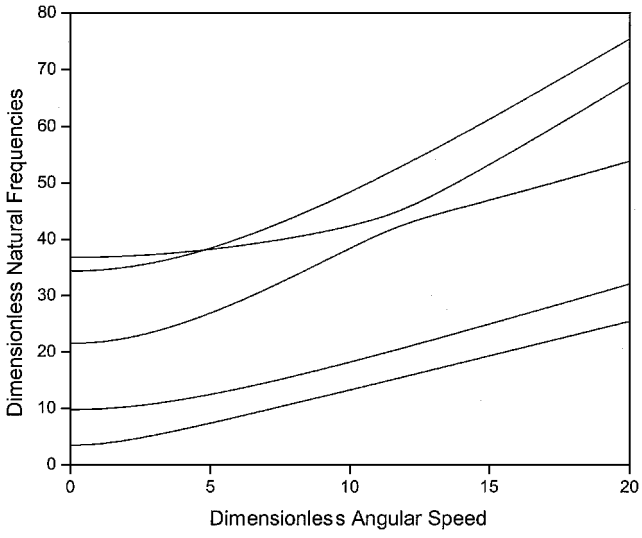

Fig. 8 Lowest five natural frequencies vs angular speed for the values of $\delta = 1.2$, $\sigma = 0.5$, and $\theta = 30$ deg.

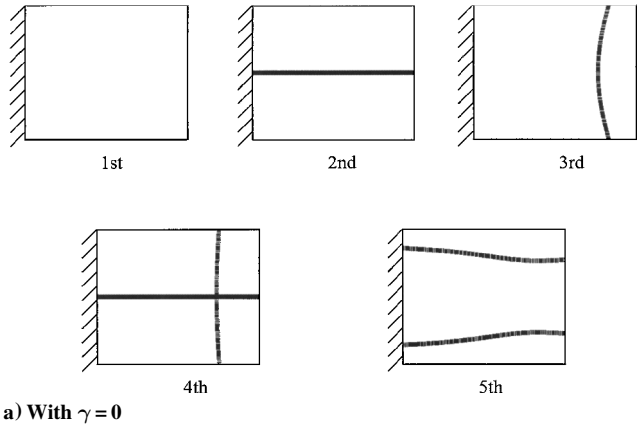

a) With $\gamma = 0$

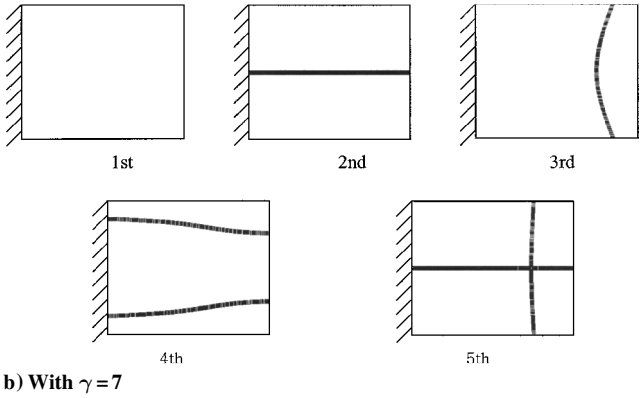

b) With $\gamma = 7$

Fig. 9 Nodal lines of the lowest five modes of a cantilever plate with $\delta = 1.2$ when angular speed $\gamma = 0$ and 7.

Figure 8 shows the variations of the lowest five dimensionless natural frequencies of rotating plates (with the aspect ratio $\delta = 1.2$, the hub radius ratio $\sigma = 0.5$, and the setting angle $\theta = 30$ deg). There are two noteworthy phenomena in Fig. 8. The first one is the crossing (around $\gamma = 5$) between the fourth and the fifth eigenvalue loci, and the second one is the veering (around $\gamma = 12$) between the third and the fourth eigenvalue loci. The veering displayed in Fig. 8 occurs gradually. In other words, the two eigenvalue loci are always substantially separated from each other. The veering phenomena observed in Fig. 6 result from aspect ratio change, that is, system configuration change. However, the veering phenomena observed in Fig. 8 can occur while the angular speed increases.

Figures 9a and 9b display the nodal lines of the lowest five mode shapes for the cantilever plate for the cases of $\gamma = 0$ and 7, respectively. In Fig. 9a, the nodal lines of the first spanwise bending mode, the first torsional mode, the second spanwise bending mode, the combination mode (torsion plus spanwise bending), and the first chordwise bending mode are shown. In Fig. 9b, however, one can observe that the fourth and the fifth mode shapes switch. This mode shape switching results from the crossing that was observed in Fig. 8. The crossing can be explained by the mode shape difference. The combination mode (compared to the chordwise bending mode) is more influenced by the centrifugal inertia force because the centrifugal inertia force, which acts parallel to the spanwise direction, influences the spanwise deformation more than the chordwise deformation. Therefore, the natural frequency of the combination mode increases faster than that of the chordwise bending mode and the crossing occurs eventually.

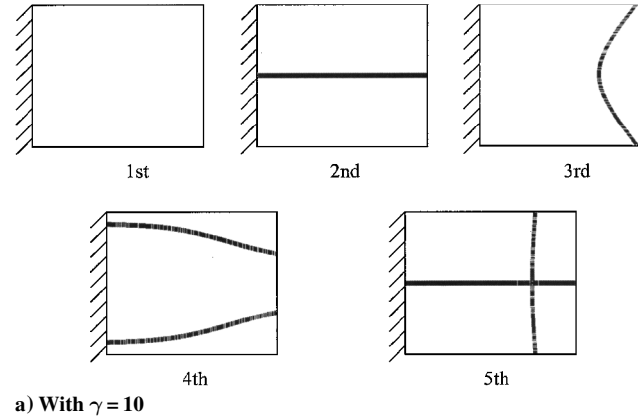

a) With $\gamma = 10$

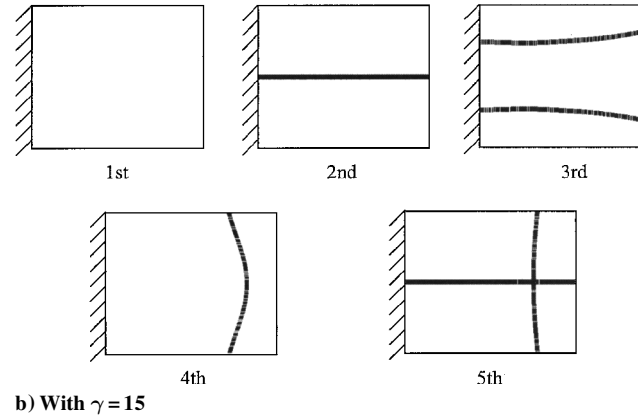

b) With $\gamma = 15$

Fig. 10 Nodal lines of the lowest five modes of a cantilever plate with $\delta = 1.2$ when the angular speed $\gamma = 7$ and 15.

Figures 10a and 10b display the nodal lines of the lowest five mode shapes for the cantilever plate for the cases of $\gamma = 10$ and 15, respectively. From Figs. 10a and 10b, one can observe that the third and the fourth mode shapes seem to switch. This switching results from the veering between the third and the fourth loci. To determine how the mode switching occurs, the variations of the third and the fourth mode shapes during the increase of angular speed are shown in Figs. 11a and 11b, respectively. When the angular speed γ is 10, the third mode shape has a nodal line in the chordwise direction, whereas the fourth mode has nodal lines in the spanwise direction. As the angular speed increases (and the two loci approach each other), all of the nodal lines become more and more bidirectional. As the angular speed increases more and eventually leaves the veering region, the two mode shapes return to the one-directional nodal line pattern except that they exchange their nodal line patterns. Also, note that the concavities of the nodal lines are reversed. Because the fourth mode has the second spanwise bending mode shape, which characterizes the third mode before the veering occurs, after leaving the veering region, the fourth locus increases faster than the third locus. Last, the nodal lines obtained in Fig. 11 are superposed in Fig. 12. Observe that two points of the plate are common to all of the nodal lines of the third and the fourth mode shapes.

Table 2 Lowest five natural frequencies for eight cases of parameter sets when $\gamma = 0$

Aspect ratio	Setting angle	First frequency	Second frequency	Third frequency	Fourth frequency	Fifth frequency
			Hub radius ratio $\sigma = 0.5$			
$\delta = 5$	$\theta = 30$	13.259	37.573	38.781	80.930	110.788
$\delta = 5$	$\theta = 60$	11.217	36.218	38.131	80.620	110.336
$\delta = 10$	$\theta = 30$	13.257	38.759	68.783	80.741	140.886
$\delta = 10$	$\theta = 60$	11.214	38.108	68.052	80.430	140.708
			Hub radius ratio $\sigma = 2.0$			
$\delta = 5$	$\theta = 30$	20.019	40.801	52.390	100.161	117.855
$\delta = 5$	$\theta = 60$	18.729	39.556	51.911	99.911	117.430
$\delta = 10$	$\theta = 30$	20.018	52.374	70.663	100.006	165.227
$\delta = 10$	$\theta = 60$	18.728	51.895	69.951	99.755	165.075

Table 3 Lowest five natural frequencies for eight cases of parameter sets when $\gamma = 20$

Aspect ratio	Setting angle	First frequency	Second frequency	Third frequency	Fourth frequency	Fifth frequency
			Hub radius ratio $\sigma = 0.5$			
$\delta = 5$	$\theta = 30$	25.444	46.271	67.573	122.225	127.405
$\delta = 5$	$\theta = 60$	21.152	41.725	66.077	121.403	125.826
$\delta = 10$	$\theta = 30$	25.444	67.562	74.005	122.100	194.308
$\delta = 10$	$\theta = 60$	21.151	66.066	71.251	121.278	193.793
			Hub radius ratio $\sigma = 2.0$			
$\delta = 5$	$\theta = 30$	39.262	55.793	96.961	148.945	167.089
$\delta = 5$	$\theta = 60$	36.627	52.085	95.924	147.597	166.488
$\delta = 10$	$\theta = 30$	39.262	80.634	96.952	166.988	230.108
$\delta = 10$	$\theta = 60$	36.627	78.114	95.915	166.388	229.237

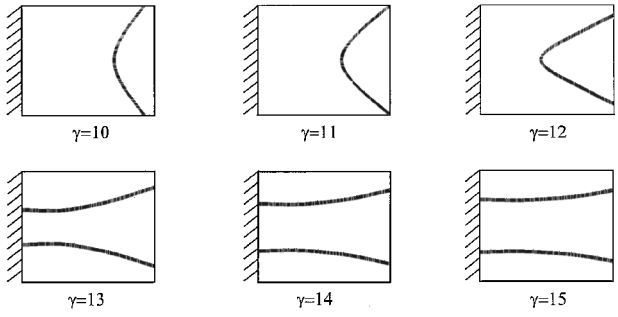

a) Third mode shape

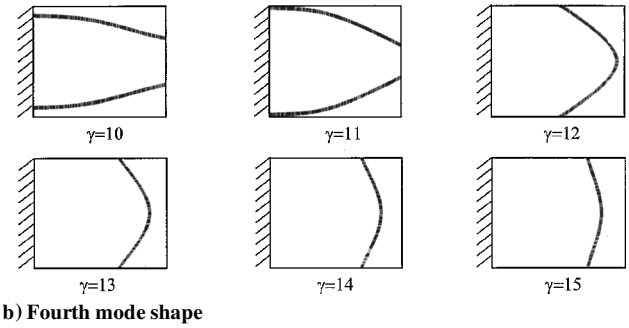

b) Fourth mode shape

Fig. 11 Variations of the nodal lines of the third and the fourth mode shapes.

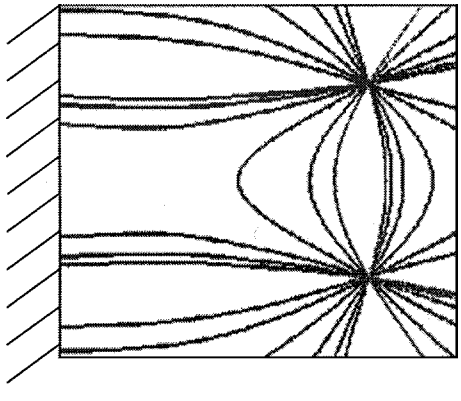

Fig. 12 Superposition of the nodal lines of third and fourth mode shapes and the existence of two common fixed nodal points.

The third mode (which is the second spanwise bending mode) and the fourth mode (which is the first chordwise bending mode) in Fig. 10 are all symmetric with respect to the horizontal line located at the middle of the plate. During the veering, the third and the fourth modes exchange their mode shapes through the continuous transformation of the mode shapes as shown in Fig. 11. Such mode shape exchange and transformation are possible because those modes are all symmetric. However, as shown in Fig. 9, the fourth mode (which is the combination mode) is skew symmetric, whereas the fifth mode (which is the chordwise bending mode) is symmetric. A veering between these two modes is impossible because a skew-symmetric mode cannot be transformed into a symmetric mode. Thus, switching from a symmetric to a skew-symmetric mode can only occur discontinuously, requiring a crossing of the loci.

Tables 2 and 3 provide the lowest five natural frequencies at two specific angular speeds for eight cases of parameter sets. Tables 2 and 3 are provided for use as benchmarks in future study.

IV. Conclusions

A modal formulation for the free vibration of a rotating cantilever plate with setting angle is presented. Three dimensionless parameters are identified through a dimensional analysis: the aspect ratio of the plate, the ratio of hub radius to plate length, and the dimensionless angular speed. The effects of the dimensionless parameters, as well as the setting angle on the natural frequencies of rotating cantilever plates, are investigated. A modal method employing assumed modes is employed to obtain numerical results. It is shown that the rotating plate's natural frequencies increase with the angular speed, that their increasing rates grow as the hub radius increases, and that the natural frequency loci are lowered by increasing the setting angle. It is also found that some natural frequencies increase faster than others as the aspect ratio or the angular speed increases. This results in the phenomena of eigenvalue loci crossing and veering. When two loci cross, the corresponding two mode shapes are simply switched and remain nearly unchanged. When two loci veer, however, mode shape variations occur continuously in the veering region. It is also observed that fixed common nodal points exist for the two continuously changing mode shapes.

Acknowledgment

This research was supported by Center of Innovative Design Optimization Technology (Engineering Research Center of Korea Science and Engineering Foundation).

References

[1]Southwell, R., and Gough, F., "The Free Transverse Vibration of Airscrew Blades," British Aeronautical Research Council, Repts. and Memoranda 766, 1921.

[2]Schilhansl, M., "Bending Frequency of a Rotating Cantilever Beam," *Journal of Applied Mechanics*, Vol. 25, No. 1, 1958, pp. 28–30.

[3]Leissa, A., "Vibration Aspects of Rotating Turbomachinery Blades," *Applied Mechanics Reviews*, Vol. 34, No. 5, 1981, pp. 629–635.

[4]Rao, J., "Turbomachine Blade Vibration," *Shock Vibration Digest*, Vol. 19, No. 5, 1987, pp. 3–10.

[5]Dokainish, M., and Rawtani, S., "Vibration Analysis of Rotating Cantilever Plates," *International Journal for Numerical Methods in Engineering*, Vol. 3, No. 2, 1971, pp. 233–248.

[6]Ramamurti, V., and Kielb, R., "Natural Frequencies of Twisted Rotating Plates," *Journal of Sound and Vibration*, Vol. 97, No. 3, 1984, pp. 429–449.

[7]Kane, T., Ryan, R., and Banerjee, A., "Dynamics of a Cantilever Beam Attached to a Moving Base," *Journal of Guidance, Control, and Dynamics*, Vol. 10, No. 2, 1987, pp. 139–151.

[8]Yoo, H., Ryan, R., and Scott, R., "Dynamics of Flexible Beams Undergoing Overall Motions," *Journal of Sound and Vibration*, Vol. 181, No. 2, 1995, pp. 261–278.

[9]Yoo, H., and Shin, S., "Vibration Analysis of Rotating Cantilever Beams," *Journal of Sound and Vibration*, Vol. 212, No. 5, 1998, pp. 807–828.

[10]Yoo, H., "Dynamic Modeling of Flexible Bodies in Multibody Systems," Ph.D. Dissertation, Dept. of Mechanical Engineering and Applied Mechanics, Univ. of Michigan, Ann Arbor, MI, April 1989.

[11]Yoo, H., and Chung, J., "Dynamics of Rectangular Plates Undergoing Prescribed Overall Motions," *Journal of Sound and Vibration*, Vol. 239, No. 1, 2001, pp. 123–137.

[12]Flower, G., "Modeling of an Elastic Disk with Finite Hub Motions and Small Elastic Vibrations with Application to Rotordynamics," *Journal of Vibration and Acoustics*, Vol. 118, No. 1, 1996, pp. 10–15.

[13]Leissa, A., "Vibration of Plates," NASA SP-160, 1969, Chap. 4, pp. 158, 159.

[14]Kane, T., and Levinson, D., *Dynamics: Theory and Applications*, McGraw–Hill, New York, 1985.

[15]Eisenhart, L., *An Introduction to Differential Geometry*, Princeton Univ. Press, Princeton, NJ, 1964, pp. 123–129.

[16]Leissa, A., "On a Curve Veering Aberration," *Journal of Applied Mathematics and Physics*, Vol. 25, No. 1, 1974, pp. 99–111.

[17]Kuttler, J., and Sigillito, V., "On Curve Veering," *Journal of Sound and Vibration*, Vol. 75, No. 4, 1981, pp. 585–588.

[18]Perkins, N., and Mote, C., "Comment on Curve Veering in Eigenvalue Problems," *Journal of Sound and Vibration*, Vol. 106, No. 3, 1986, pp. 451–463.

E. Livne
Associate Editor